Hindawi
Advances in Civil Engineering
Volume 2020, Article ID 8863547, 11 pages
https://doi.org/10.1155/2020/8863547

*Research Article*

# Rupture and Migration Law of Disturbed Overburden during Slicing Mining of Steeply Dipping Thick Coal Seam

**Shuai Liu**,[1,2,3] **Ke Yang**,[2,3] **Chunan Tang**,[1,4] **and Xiaolou Chi**[2,3]

[1]*School of Resources and Civil Engineering, Northeastern University, Shenyang 110819, China*
[2]*Institute of Energy, Hefei Comprehensive National Science Center, Hefei 230031, China*
[3]*State Key Laboratory of Mining Response and Disaster Prevention and Control in Deep Coal Mines, Anhui University of Science and Technology, Huainan 232001, China*
[4]*School of Civil and Hydraulic Engineering, Dalian University of Technology, Dalian 116024, China*

Correspondence should be addressed to Ke Yang; keyang2003@163.com

Received 27 August 2020; Revised 13 September 2020; Accepted 23 September 2020; Published 8 October 2020

Academic Editor: QiFeng Guo



Steeply inclined and thick coal seams in Huainan Panbei Coal Mine in Anhui Province, China, were analyzed by physical analog modeling, acoustic emission (AE), and distributed fiber sensing (DBS). The secondary deformation breakage law, sound, and light response characteristics in the rock mass deformation process induced by lower slice mining of steeply inclined coal seams were determined. The results show that the mutation of the hinged rock beam structure in the lower region and the cantilever beam structure in the upper region of the lower slice disturbed overburden is the main cause of the rupture of the workface roof. Based on the AE energy and distributed fiber strain response characteristics, the six stages of disturbed overburden instability in the lower slice and cyclic patterns of steeply inclined coal seams were revealed. The key prevention and control areas of the workface were found to be related to the disturbed high-level immediate roof rupture during the lower slice mining process, rupture of the disturbed main roof, and sliding of disturbed overburden. The three-stage AE positioning morphological characteristics and DBS response stepped jump patterns were analyzed in detail. The research results are considered instrumental in the combined AE and DBS monitoring of deformation and damage of rock and soil structures.

## 1. Introduction

Coal seam mining causes overburden movements, which can jeopardize coal production safety. Therefore, mining-caused overburden movement patterns are vital for mining technology [1]. However, due to the high cost of field research, limitations of monitoring equipment, and other factors, the overburden deformation and rupture laws are mainly determined by the physical analog modeling (PAM). This is a robust laboratory technique for reproducing, at small scale, geometric and kinematic features of natural geologic structures by a proper selection of deformation styles and analog materials. The latter include sand, claycake, silicon putty, and so forth and simulate rock strata table-top scale analog layers. Under the condition of satisfying the basic similarity principle, PAM can accurately reflect the engineering structure relationship. Because of its unique superiority, it is widely used in geotechnical engineering [2, 3]. Many scholars have used PAM to analyze the gangue slip filling characteristics after rupture of steeply inclined coal seams overburden. They studied the dip and antidip directions' pile structure in the process of steeply inclined coal seams workface gangue slip, obtained asymmetric "ruptured arch" of steeply inclined coal seams overburden, and revealed the asymmetric "arch shell" form of overburden space mining by steeply inclined coal seams [4, 5, 6, 7, 8, 9]. However, due to the coal seam occurrence conditions and mining technology impacts, in steeply inclined and thick coal seams sliced mining, the overburden structure changes under the influence of multiple mining. Given this, the laws of

disturbed overburden rupture and migration after overburden structural change in steeply inclined coal seams mining are very topical.

The PAM approach envisages deformation monitoring via total stations, dial gauges, strain gauges, and so forth, whose testing accuracy and sensitivity need further improvement: most of them use point monitoring, while the layout of points and lines is too complicated. In general, deformation monitoring can only monitor the model's surface but fail to implement internal monitoring. With the rapid development of acoustic emission (AE) nondestructive detection technology, numerous researchers had successfully used it to detect the number of events and energy rates of the PAM when the chasm slips were unstable [10]. They obtained the precursor information of chasm instability and revealed the characteristics and dynamic response laws of stope pressure before and after the activation of chasms [11]. Besides, the AE technology was also utilized in the assessment of characteristics of the spatial-temporal evolution of dynamic instability of large-inclination coal and rock masses [12, 13, 14, 15, 16]. Another hot field of research is fiber sensing technology, which can achieve long-distance distributed monitoring. Using the advantages of anticorrosion, antielectromagnetic interference, small size, lightweight, high sensitivity, high precision, and so forth, it ensures the stability monitoring for geotechnical [17, 18], geology [19, 20], water conservation [21], aerospace [22], defense [23], and other applications. References [24–26] incorporated the optical fiber sensing technology into the logical/physical model to monitor the deformation and weighting of workface overburden, which yielded interesting findings. This technology has been successfully applied to the monitoring of overburden migration in coal mine goaf [27, 28].

In this study, the PAM, AE, and distributed fiber sensing (DBS) are jointly applied to steeply inclined coal seams for assessing the disturbed overburden secondary deformation and rupture patterns, as well as the characteristics of sound and light response in the process of rock deformation and rupture. This research can provide a theoretical reference for the prevention of hazards such as rib spalling, roof falling, and support instability. The research results are considered instrumental in the AE and DBS detection of rock and soil structure deformation and damage.

## 2. Principles of Acoustic and Optical Detection Methods

*2.1. AE-Based Positioning by Time Differences.* Positioning by time differences is aimed to determine the sound source's coordinates or position by measuring the parameters of each AE channel signal TDOA, wave speed, and sensor spacing and their processing via a certain algorithm. This accurate yet complicated positioning method has been widely applied in component detections. When performing planar positioning on a diamond array composed of four AE sensors, AE can obtain a real positioning sound source, as shown in Figure 1. In actual component AE monitoring, the number of AE sensors often exceeds four. If an individual AE sensor fails during monitoring, the remaining four AE sensors can still monitor a real positioning sound source.

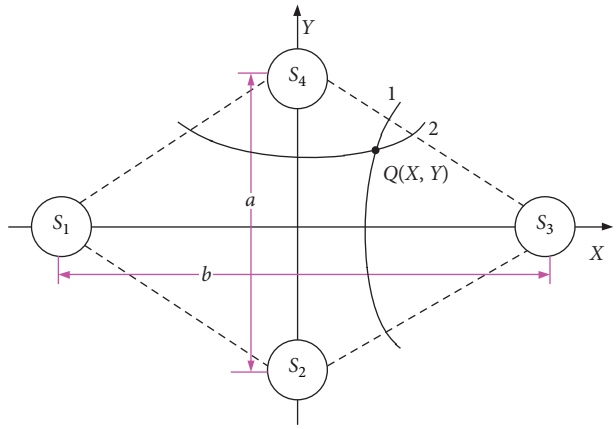


Figure 1: The AE sound source positioning of an array composed of four AE sensors.

Assume that the hyperbolic curve 1 is obtained from the time difference $\Delta t_X$ between $S_1$ and $S_3$ AE sensors, the hyperbolic curve 2 is obtained from the time difference $\Delta t_Y$ between $S_2$ and $S_4$ AE sensors, the positioning sound source is $Q$, the distance between $S_1$ and $S_3$ sensors is $a$, the distance between $S_2$ and $S_4$ sensors is $b$, and the wave velocity is $V$. Then, the positioning sound source is located at the intersection point $Q$ $(X, Y)$ of the two hyperbolae, and its coordinates can be expressed as follows:

$$X = \frac{\Delta t_X V}{2a}\left[L_X + 2\sqrt{\left(X - \frac{a}{2}\right)^2 + Y^2}\right],$$
$$Y = \frac{\Delta t_Y V}{2b}\left[L_Y + 2\sqrt{\left(Y - \frac{b}{2}\right)^2 + X^2}\right]. \quad (1)$$

*2.2. Optical Fiber Sensing Measurements.* DBS uses optical fibers as sensing elements. When the measured fiber is subjected to an external force or temperature variations, the frequency of the stimulated Brillouin scattered light in the fiber will change. The strain data transferred along the fiber can be obtained by conversion. The relationship between the Brillouin frequency shift, temperature, and strain is [29]

$$\Delta\varepsilon = \frac{(\Delta V_B - C_1 \Delta T)}{C_2}, \quad (2)$$

where $\Delta V_B$ is Brillouin frequency shift, MHz; $C_1$ is temperature sensitivity coefficient, MHz/°C; $C_2$ is strain sensitivity coefficient, MHz/$\mu\varepsilon$; $\Delta T$ is temperature variation, °C; and $\Delta\varepsilon$ is strain variation. This method is based on the principle of light scattering and measures the frequency change of Brillouin scattered light.

It is generally believed that when the temperature variation is within 5°C, the Brillouin frequency shift caused by the temperature can be ignored. In this study, this test is

carried out indoors, and the measured temperature variation is less than 3°C. Therefore, the temperature effect on the measurement results can be ignored.

## 3. Physical Analog Modeling Procedure

*3.1. Case Study.* The experiment uses 12123 working face of the Huainan Panbei Coal Mine in Anhui Province, China, as the engineering geological case study. The main coal seam is #13–1 coal seam, the average seam inclination angle is 40°, the average thickness is 4.4 m, and inclined mining in slices is adopted. The upper slice has a mining height of 2.0 m and a surface length of 120 m. Recovery was completed in 2015. The lower slice has a mining height of 2.4 m and a surface length of 90 m. The recovery interval between the upper and lower slices is two years. The lower slice is arranged in the middle and lower parts of the goaf in the upper slice. Specifically, the lower slice's gate road is 5.0 m away from the gate road in the upper slice. Figure 2 is a schematic diagram of the location and production conditions of 12123 working face. The coal seam hardness coefficient ($f$) is 0.3~0.5, the immediate roof is the interslice of mudstone and sandy mudstone, and the average thickness is 9.3 m. The immediate floor is mudstone, and the average thickness is 3.0 m.

*3.2. Physical Analog Model (PAM).* The test uses a rotating plane PAM frame; the device dimensions are length × width × height = 2.0 m × 0.2 m × 2.0 m. PAM requires that each part's size is enlarged or reduced according to a uniform ratio between the physical model and the prototype, which is $l_m/l_p = C_l$. According to the 12123 working face engineering geological data and test device dimensions, we determined the geometric similarity constant $l_m/l_p = C_l = 100$, bulk density similarity constant $C_\gamma = \gamma_p/\gamma_m = 1.6$, stress similarity constant $C_\gamma = C_{\gamma.}$ $C_l = 160$, and time similarity constant $C_\tau = C_l^{1/2} = 10$. In the above similar constant formulas, the subscript parameters $p$ and $m$ represent the prototype and model, respectively.

The test uses river sand as aggregate, gypsum, lime as cementing material, and water as the bonding material. Due to the article's limited space, the detailed similar material ratio and modeling process are omitted and can be found elsewhere [30, 31]. Based on the similarity constant and the physical and mechanical parameters of coal, the weighted mixing test between the above analog materials was used to adjust and determine the similarity ratio and then calculate the proportions of analog materials in each coal slice. Analog materials are also stirred, laid, and compacted slice by slice. Different colors are sprayed on different rock slices of the high-level floor of the workface to distinguish them. The physical and mechanical parameters of coal and similar materials are listed in Table 1.

The test laying height is 1.5 m, and the workface burial depth ranges from −375 to −495 m. After the overlying nonsimulated rock slice is converted by a load similar constant, the top of the physical model is loaded by a multifunctional adjustable PAM loading device. The complete physical model is depicted in Figure 3.

*3.3. Monitoring System.* Coal pillars of 50 cm are left on each side of the upper slice. The upper and lower simulation slices' excavation distance is 10 cm, the upper slice is excavated 12 times, and the lower one is excavated nine times; each excavation duration is about 1 min. The interval of each excavation is 20 min.

Steeply inclined coal seams are generally cut from top to bottom, and the frame is moved from bottom to top. When the rock slice is broken, the slippage mainly occurs during the frameshift phase. Therefore, the bottom-up simulation of coal cutting is adopted in the two-dimensional physical model. Six AE sensors, numbered $P_1$–$P_6$, are embedded beforehand in the physical model, to facilitate the picking of 3D positioning points. Among them, $P_1$, $P_3$, and $P_5$ are embedded in the front, while $P_2$, $P_4$, and $P_6$ are implanted in the back. The specific locations are shown in Figure 4. Before the workface simulation recovery, the AE parameters need to be calibrated, and the upper slice recovery process is used to check the accuracy of the AE parameters. The AE sensor's resonance frequency is finally determined to be 100–600 kHz, the sampling rate is 3 MHz, the preamplifier gain is 40 dB, and the monitoring threshold is 90 dB. With such AE parameters, the AE signal is not affected by the excavation action, which is convenient for later data screening. When the lower slice is excavated, the AE is turned on synchronously until the overburden structure is stable.

The distributed fiber uses a high-transmission low-rigidity responsive sensing optical cable with a 2 mm diameter, and the fiber placement is shown in Figure 4. The optical fiber is embedded in analog materials. To make the optical fiber tight, a certain pretightening force is applied to both optical fiber ends. A small amount of cement slurry is put to make it tightly coupled with analog materials. Like AE parameter calibration, optical fiber also needs to be calibrated for strain coefficient accuracy. For brevity sake, a detailed calibration process can be found elsewhere [32]. The spatial resolution of the optical fiber strain measurement is set to 50 mm. The optical fiber can monitor the rock slice's deformation and rupture before and after the overburden structure disturbance in the upper and lower slices on a real-time scale. The optical fiber strain's positive and negative values indicate that the analog material is in a stretched and compressed states, respectively. The physical model is installed in front of the camera to monitor the rock deformation and rupture.

## 4. Results and Discussion

*4.1. Rock Slice Rupture and Migration Features.* After the upper slice excavation, the immediate roof breaks at the height of 9.3 m, and the gangue moves down along the floor of the workface. The gangue's nonuniform filling characteristics are enhanced, showing the goaf filling with an "upper empty, middle full, and down solid" feature. The immediate high-level roof has a macrofracture (crack line in *A-A* red frame), and the rock slice below the fracture surface loses its bearing capacity. In contrast, a stable cantilever beam structure (*A-A* red frame) is formed above the fracture surface, which has a certain bearing capacity. In the workface

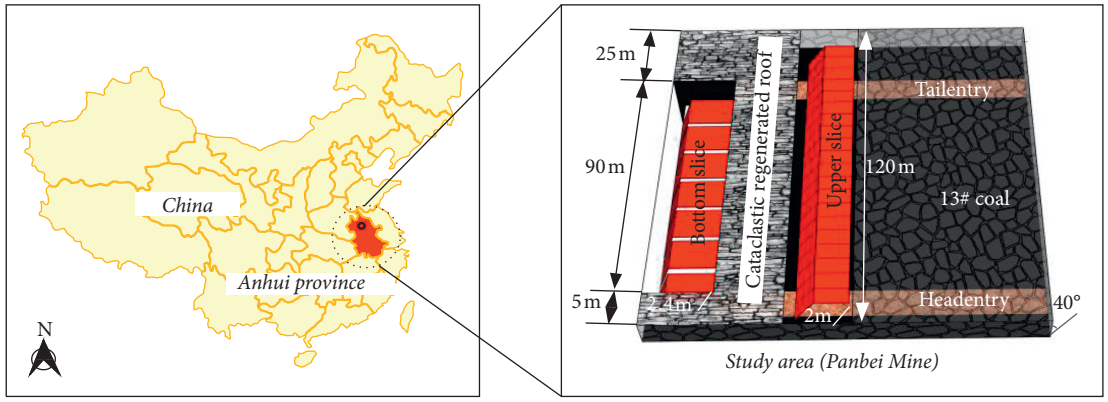


Figure 2: The location and production conditions of 12123 working face.

Table 1: Rock physical and mechanical parameters and similarity ratios.

| Rock property | Compressive strength (MPa) | Elastic modulus (GPa) | Cohesion (MPa) | Internal friction angle (°) | Poisson's ratio | Similarity ratio | Mass (kg) | | | |
|---|---|---|---|---|---|---|---|---|---|---|
| | | | | | | | Fine river sand | Lime | Gypsum | Water |
| Medium sandstone | 57.86 | 18.00 | 2.41 | 35 | 0.20 | 6 : 6: 4 | 35.12 | 3.51 | 2.34 | 4.10 |
| Fine sandstone | 70.08 | 15.32 | 2.68 | 38 | 0.15 | 6 : 6: 4 | 34.48 | 3.45 | 2.30 | 4.02 |
| Sandy mudstone | 35.63 | 9.51 | 1.22 | 30 | 0.28 | 7 : 7: 3 | 47.70 | 4.77 | 2.04 | 5.45 |
| Mudstone | 21.52 | 6.24 | 0.95 | 24 | 0.30 | 10 : 7: 3 | 14.23 | 1.00 | 0.42 | 1.56 |
| 13–1#coal | 13.46 | 5.83 | 0.62 | 20 | 0.35 | 10 : 5: 5 | 35.10 | 1.76 | 1.76 | 3.86 |
| Mudstone | 21.52 | 6.24 | 0.95 | 24 | 0.30 | 10 : 7: 3 | 16.27 | 1.14 | 0.49 | 1.79 |
| Sandy mudstone | 35.63 | 9.51 | 1.22 | 30 | 0.28 | 7 : 7: 3 | 29.15 | 2.92 | 1.25 | 3.33 |

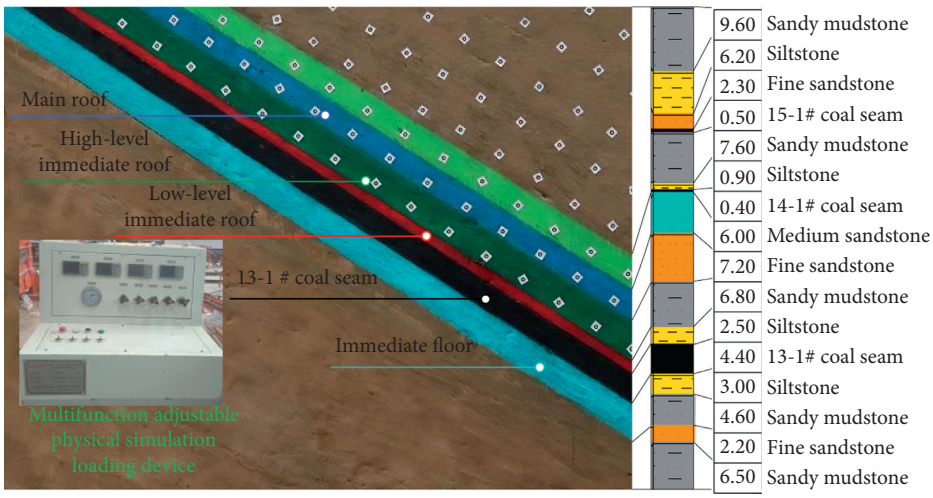


Figure 3: Physical analog model.

lower area, the gangue piles up, the overburden's movement space in the mined-out area decreased, and overburden shows transverse and longitudinal cracks and delamination [33, 34]. It is still not completely separated from the stable rock slice and has the form of a hinged rock beam structure. Its load directly acts on gangue (or bracket). According to the time similarity constant, after the upper slice overburden is stabilized, continue to excavate the lower slice, as shown in Figure 5. After the lower slice's excavation, there is a free space height below the disturbed overburden, and the

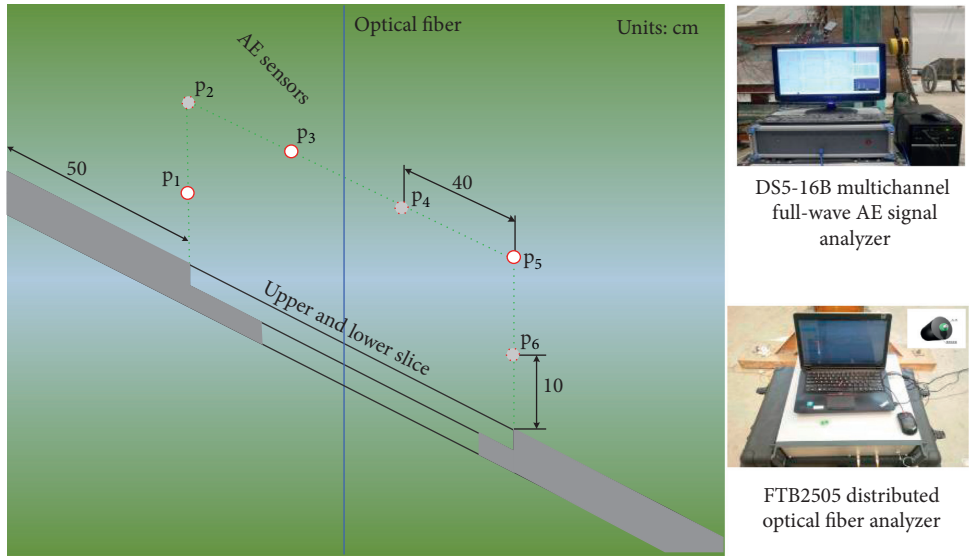


Figure 4: Monitoring system.

gangue's ability to restrain the disturbed overburden is weakened. Under the superposition of overburden gravity and mining stress, the hinged rock beam formed by disturbed overburden breaks and slips after "activation." The disturbed overburden structure is changed.

Specifically, the overlying low-level disturbed overburden (*B–B* middle and lower parts sprayed with red and dark green) emerges during mining, which exposes the high-level disturbed overburden above it. Gangue slides along the workface floor to fill the lower part of the goaf, while the free space below the disturbed overburden in the middle and upper parts of the goaf (available for the rock slice to break and rotate) increases. The disturbed overburden breaks up to the main roof (B′-B′ part sprayed with dark blue paint). The breaking height is 16.5 m. After the simulated excavation reaches the upper end of the lower slice, the structure of the cantilever beam formed after the upper slice excavation is unstable and together with the disturbed overburden above the coal pillar has slip damage without any support (A′-A′ red frame), with the development of coal pillar cracks and severe gangling (A′-A′ yellow frame).

Comprehensive analysis shows that, during the lower slice recovery process, the disturbed overburden is severely broken under the secondary mining action, and it is very easy to induce the roof collapse, which causes the bracket to be improperly connected, and the bracket falls, slips, reverses, and becomes unstable. For the lower slice return airway, the first required measure is to prevent the roof from breaking, and the second one is to avoid the breaking impact of the cantilever beam formed by the high immediate roof above the coal pillar on the support after the upper slice recovery.

*4.2. Rock Slice Rupture AE Response.* The physical analog model has a large scale, and the distance between the AE sensors is relatively large. According to a single AE sensor, it is difficult to obtain the AE response law of distorted overburden deformation and rupture. Hence, based on the time node after disturbed overburden structure mutation of lower slice mining, the data of six AE sensors are synthesized to extract the parameters, such as energy and ring count, and are recorded as the number of one event. The 3D positioning (AE events) in the gangue sliding process is relatively random. Only the 3D positioning AE data of the disturbance caused by high roof breaking, rupture of the disturbed main roof, and sliding of disturbed overburden are extracted. Energy is a relative value monitored by the AE analyzer per unit time and is an important indicator of the fracture rate and size of the rock mass; the ring count is the cumulative value monitored by the AE analyzer per unit time and is an important indicator of the rock mass destruction.

Figure 6 depicts the relationship between the break and slip of the lower slice disturbed overburden and time. During the lower slice recovery process, primary cracks in the disturbed overburden continue to develop, a large amount of elastic energy accumulating at the crack tip and its surroundings.

The AE energy gives rise to six higher-energy bundles. The first energy peak of the AE multimodal energy bundle is the largest. Then, the peak value gradually decreases within the duration of each disturbed overburden break, or it appears as a single peak. It shows that the instability of the lower slice disturbed overburden has gone through six stages, and when the disturbed overburden breaks in each stage, the first break strength is the largest. The first energy bundle appears when the disturbed low-level immediate roof (B–B part painted in red in Figure 5) is broken. The elastic wave released by the broken overburden at this stage is low, and its duration is shorter. The peak value of AE energy is 778.3 mV·mS, and the cumulative ring count increases slowly. The second energy bundle appears when the disturbed high-level immediate roof (B–B part painted in dark green part Figure 5) is broken. At this stage, the peak value of AE

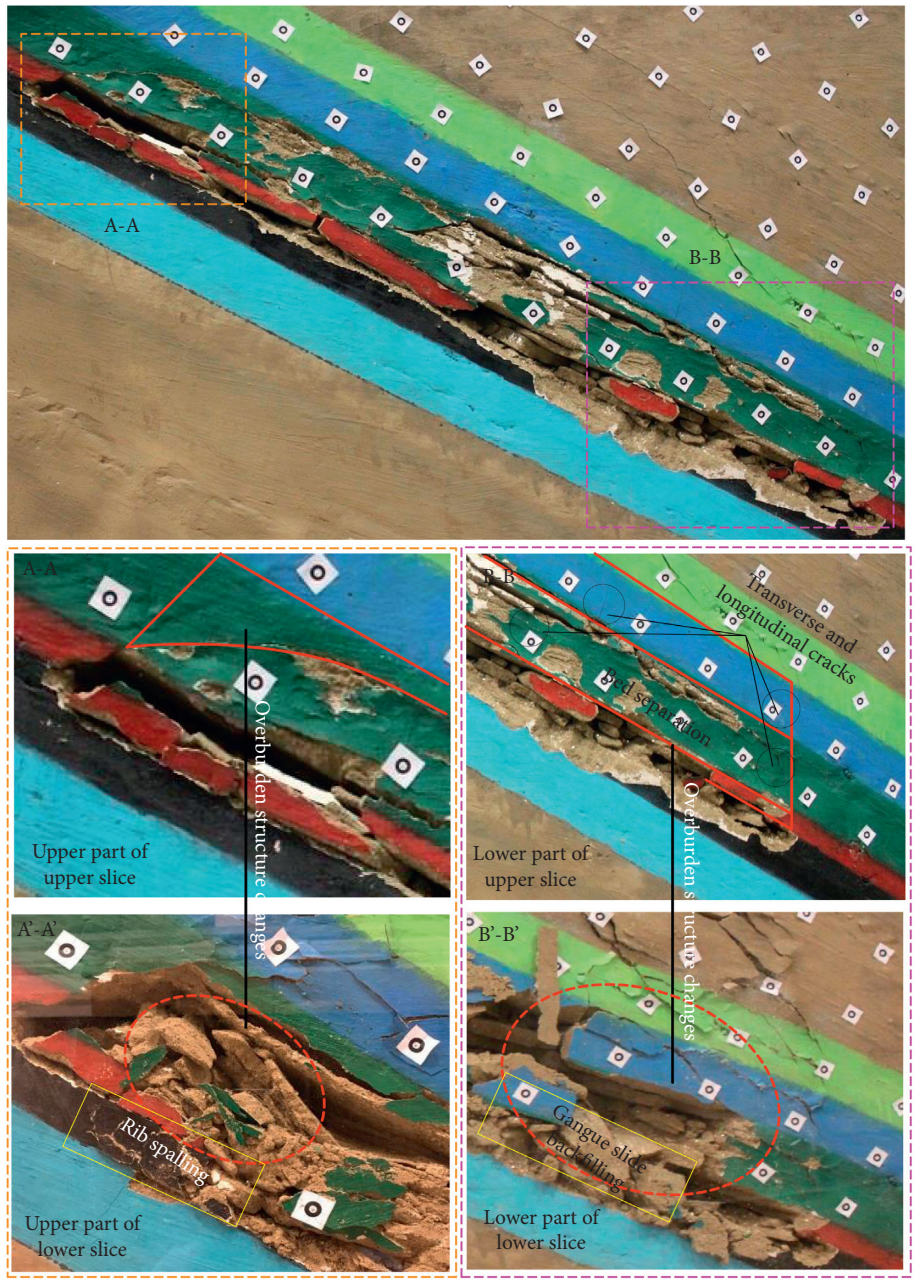


Figure 5: Workface overburden structure variation stages.

energy shows a "group shock" phenomenon. The highest peak value reaches 4973.1 mV·mS, the duration is 38 s, the cumulative ring count jumps from 2867 to 3631, and the total number of events in this stage is 2462 *n*. The third energy bundle appears when the gangue slides along the workface floor after the disturbed high-level immediate roof is broken. The lower slice's gangue is stacked, the free space height in the middle and upper regions increases, and the exposed length of the disturbed main roof increases. The fourth energy bundle appears when the exposed disturbed main roof (BB sprayed blue part in Figure 5) breaks. At this stage, the peak value of AE energy is "isolated." The isolated peak value of AE is 3914.3 mV·mS. The duration is 3s, the cumulative ring count jumps rapidly from 4541 to 5574, and the total number of events at this stage is 726 *n*. This shows that the rock breakage at this stage is "abrupt."

After the rock slices at the first and second stages are broken, gangue has filled the lower and middle parts of the lower slice. The space available for gangue slippage after the fourth stage rupture of the disturbed main roof is reduced; that is, the fifth energy bundle caused by gangue slippage is weak and exhibits a "solitary shock" form. When the upward simulation excavation reaches the upper part of the lower slice, the disturbed overburden above the coal pillar breaks and slips under the joint action of overburden load and mining stress. The sixth energy bundle emerges. The highest energy peak is 3801.5 mV·mS, the duration is 11 s, the

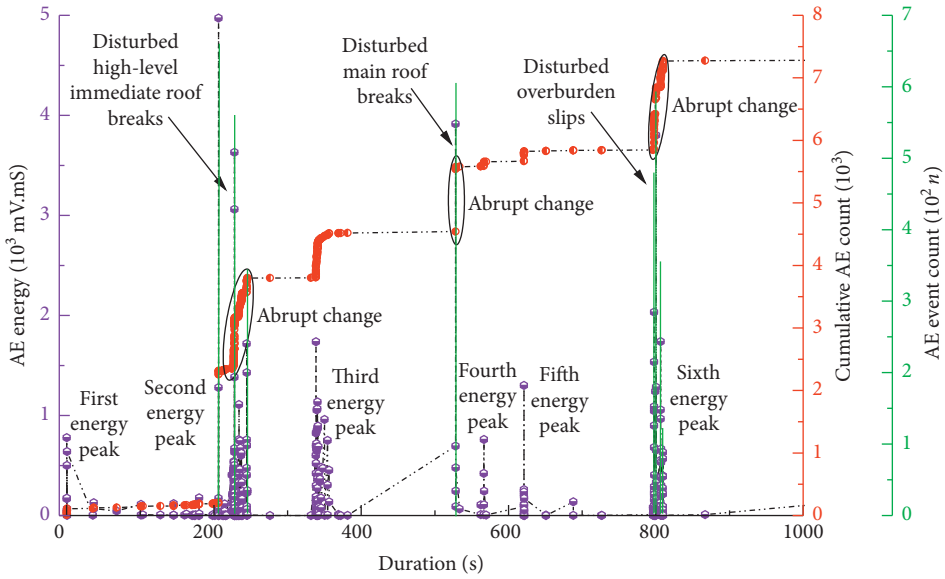


Figure 6: Relationship between disturbed overburden breaking and slipping AE parameters and time.

cumulative ring count jumps from 5854 to 7270, and the total number of events is 2084 $n$.

The procedure requires breaking the disturbed high-level immediate roof, importing the 3D positioning AE data of the rupture of the disturbed main roof, and sliding the disturbed overburden into AutoCAD software to generate 3D positioning line drawings and perform postprocessing such as coloring. Figure 7 shows the spatial positioning pattern of the generated disturbed overburden breaking AE signals. As observed, the distribution of AE spatial positioning points is roughly corresponding to the broken position of the disturbed overburden (A′-A′, B′-B′ red box in Figure 5) in the lower slice. Disturbed high-level immediate roof breaking off locations of AE in the space are more scattered, mainly extending from the location of the disturbed high-level immediate roof to the surrounding area, showing the relative ductility destruction of the disturbed high-level immediate roof rock slice. Rupture of disturbed main roof AE positioning points is concentrated in space, showing the relative brittleness damage of disturbed main roof. After simulating the excavation of the lower slice's upper area, disturbed overburden damage, and slips, the AE space positioning points are distributed in a "flow-like" way.

The comprehensive analysis revealed that macro- and microcracks in the disturbed high-level roof were more developed. Under the superimposed action of overburden load and mining stress, macro- and microcracks continued to store elastic energy. When the energy storage limit was reached, the disturbed high-level immediate roof breaking lasted for a long time, and the energy released was quite high (the second energy bundle). However, the amount of energy released per unit time was relatively small. The internal cracks in the rock slice had sufficient time to evolve and develop. The distribution of 3D positioning points was divergent, and the damage degree of the rock body was increased. The rock body was broken, and the broken gangue moved violently in the lower slice goaf (or support top beam). Disturbed main roof macro- and microcracks were not developed. Under the superimposed action of overburden load and mining stress, the macro- and microcracks released higher energy after reaching the energy storage limit in a short time (the fourth energy bundle). The cumulative ringing count per unit time exhibited a sharp jump, and the rock mass was quickly fractured. The internal structure of the rock slice had no time to evolve and was damaged. The distribution of 3D positioning points was aggregated, and the overall damage degree of the rock body was small. The disturbed main roof possessed the characteristics of sudden damage and could produce the impact-caused instability to the lower sliced support. When the simulated excavation reached the lower slice's upper part, the disturbed overburden slips, but its integrity after fracture was high. The distribution of 3D positioning points was streamlined. The cumulative value of the ringing count in the disturbed overburden slipping process per unit time was between the value of disturbed high-level immediate roof process and the value of rupture of disturbed main roof process.

*4.3. Rock Rupture Fiber Response.* The first mining of the upper slice (advance of 10 m) is detected by optical fiber sensing, indicating that the fiber senses the weak deformation inside the rock slice. As shown in Figure 8(a), when the upper slice excavation is simulated, the fiber response shows a "double peak" shape, and peak sizes are 436 and 534 $\mu\varepsilon$, respectively. The corresponding physical model heights are 680 and 980 mm, respectively. The fiber response double peak position is projected onto the upper slice workface, which is mainly located in the middle and upper regions of the upper slice. After the steeply inclined coal seams mining, the overburden in the upper part of the workface breaks and slips. The gangue fills the lower part of the workface, hindering the continued breakage of the overburden in the lower part of the workface. There is a high

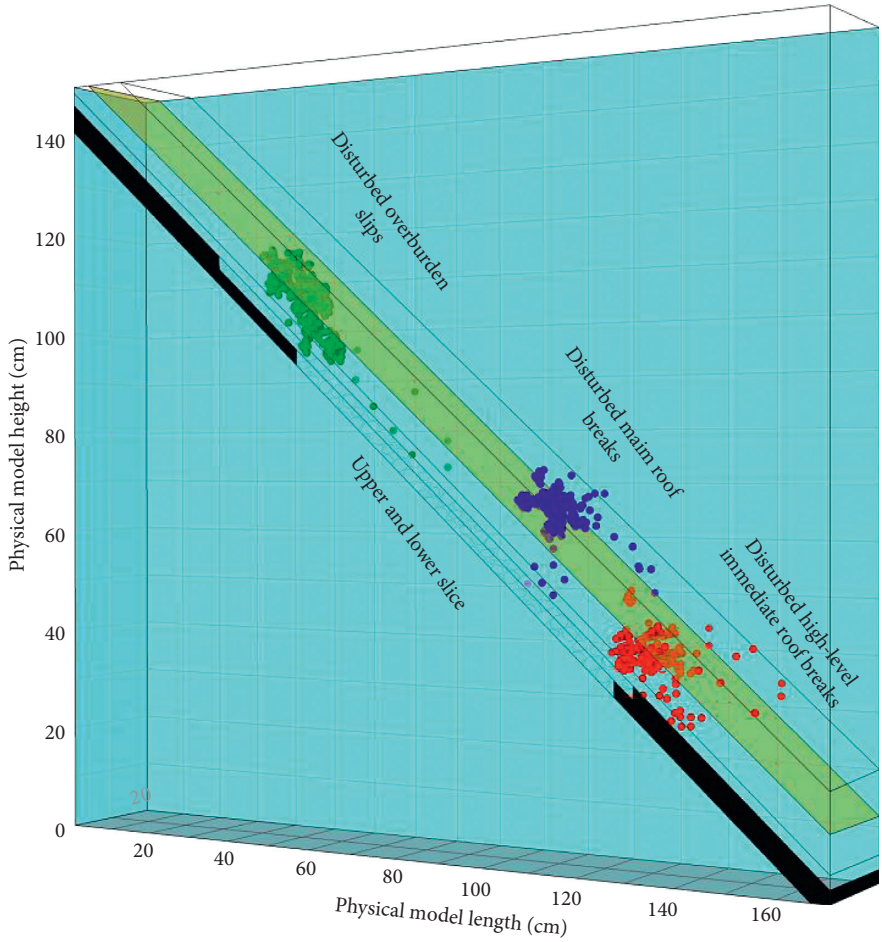


Figure 7: Disturbed overburden rupture AE spatial positioning pattern.

peak fiber response in the upper part of the workface and a small peak response in the lower part, further explaining the asymmetric feature of steeply inclined coal seams workface overburden breakage.

Taking the fiber response before and after the disturbed high-level immediate roof breakage as an example, the optical fiber response change characteristics before and after the lower slice disturbed overburden breakage are analyzed, and the results are shown in Figure 8(b). As observed, before the lower slice disturbed high-level immediate roof breaks, the tensile stress concentration occurs in the disturbed overburden (the fiber response value is positive), and the elastic deformation in the rock gradually accumulates. The peak value of the optical fiber response is 2095 $\mu\varepsilon$, and the peak position is located above the breaking line of the disturbed high-level immediate roof, while the height of the corresponding physical model is 673 mm. After an immediate high-level roof of the disturbed lower slice is broken, the rock mass in the fiber-implanted slice shows a certain degree of stress release, and the accumulated elastic strain energy is also released. The optical fiber response's peak value drops from 2095 to 1717 $\mu\varepsilon$, and the peak position is the same as before the disturbed high-level immediate roof breakage. This is consistent with AE's response law before and after the breakage of the disturbed high-level immediate roof (the AE energy accumulation in the rock before the breakage, and the release of AE energy after the breakage). For the rupture of the disturbed main roof and disturbed overburden, the fiber response before and after the slip also follows the same pattern (more detailed analysis is omitted for brevity). The critical point on the optical fiber response curve in the whole process of the lower slice simulation excavation from monotonous increase to monotonous decrease is roof breaking. The instantaneous response before breaking reaches the maximum value. After breaking, the roof rock slice quickly releases pressure, and stress is transferred to the deep stable rock mass around the goaf. At this time, the roof rock slice's stress at the breaking position reaches the minimum value, and the overburden movement gradually stabilizes. After that, as the work surface advances, it monotonically increases again, and the process forms the work surface with a periodic mineral pressure trend. The cycling process forms the appearance of the workface's periodic mineral pressure along the inclined workface.

During the lower slice simulation excavation, the optical fiber response data after the disturbed high-level immediate roof rupture, rupture of the disturbed main roof, and disturbed overburden slipping are extracted, as shown in Figure 8(c). As observed, after the rupture of the disturbed high-level immediate roof, the rock slice is

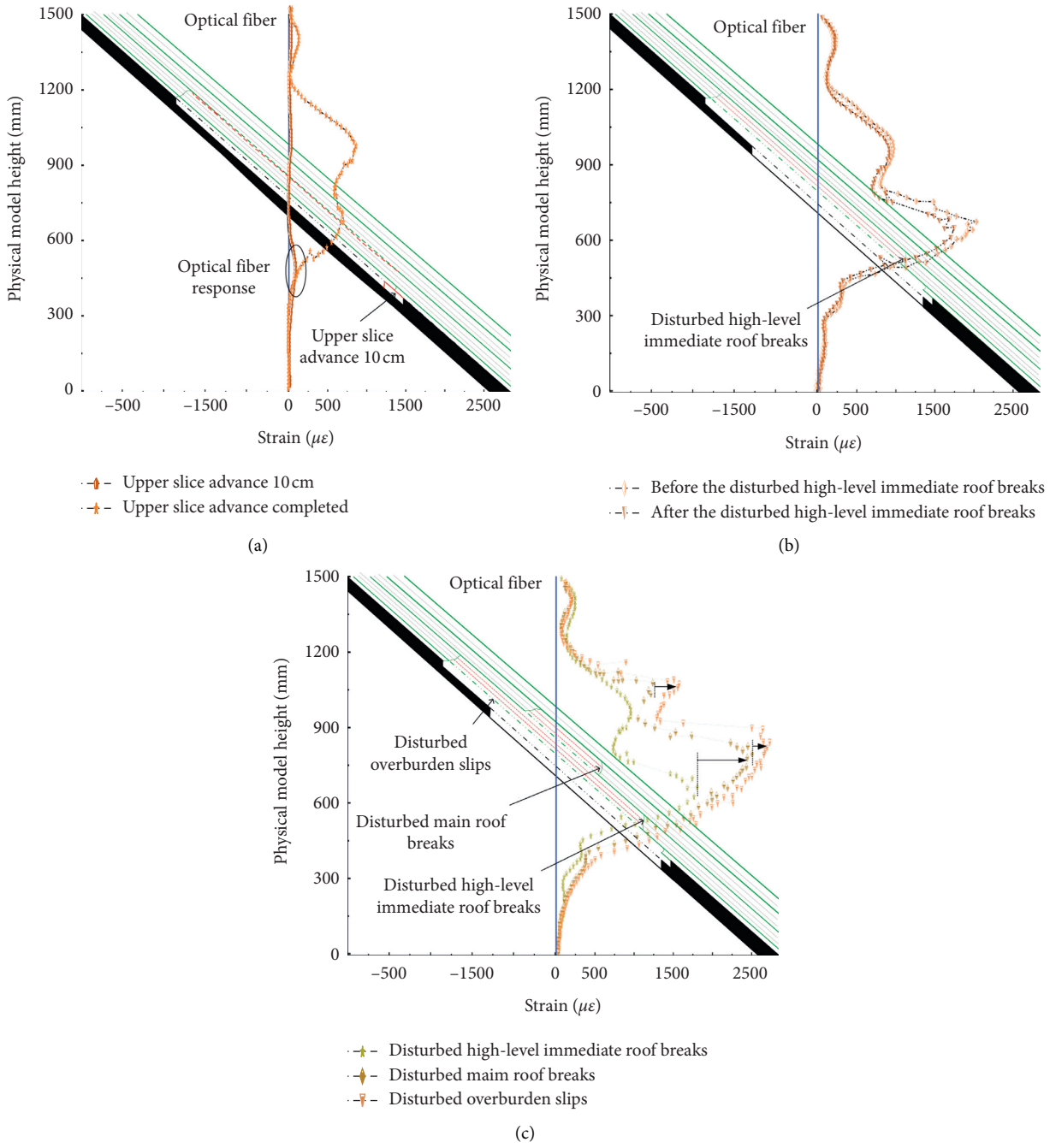


FIGURE 8: Roof fall fiber response characteristics: (a) Upper slice recovery fiber response, (b) disturbed high-level immediate roof rupture fiber response, and (c) rock rupture in the lower strata in different regions of fiber response.

opened to form a separation crack, which causes the tensile stress concentration in the optical fiber. With the upward excavation of the PAM and the rupture of the disturbed main roof, the optical fiber response's peak value jumps from 1717 to 2547 $\mu\varepsilon$ in steps. The peak position is located above the line of the rupture of the disturbed main roof. The specific height of the corresponding PAM is 796 mm. With the simulated excavation of the lower slice's upper area, the optical fiber senses the disturbed overburden slip in the upper area of the lower slice, and the peak value of the optical fiber strain also shows a stepped jump of 1575 $\mu\varepsilon$. The peak position corresponds to the PAM height of 1078 mm. The distributed fibers monitor the process of abscissa slice development, expansion, closure, rebirth, and so forth. The abscissa slice development length gradually expands, as the lower slice progresses upward along the inclination.

The sandstone in the upper part of the lower slice (A′-A′ and B′-B′ sprayed green part in Figure 5) does not change significantly in the subsequent excavation process, indicating that the upper part sandstone constitutes the main key slice of the physical model.

*4.4. Substantiation of Three Key Protection Areas in the Lower Slice by Fiber Sensing and AE Methods.* The AE and distributed fiber monitoring results inevitably have errors. PAM has a plane stress state from an experimental perspective, and constraints do not effectively control its surface. The brittle sand material affects the contact area of the sensor and the effective transmission of strain data. From the perspective of AE and fiber sensing technology, the broken rock slice leads to incomplete contact between the sensor and rock slice, causing slippage and shedding. All these factors may bring uncertainty to the measurement. Although different sound and light measurement methods have certain differences in specific values, the overall regularity is not changed. It is necessary to analyze the influencing factors in further research and eliminate them gradually.

Under the influence of secondary mining, the lower slice disturbed overburden slips, and the lower slice's return airway is seriously damaged. The disturbed main roof in the central area of the workface breaks "suddenly," which has a positive impact on the bracket and may cause the bracket to fall, slip, and become unstable. The disturbed high-level immediate roof in the lower area of the workface breaks, the gangue slides down along the floor of the workface, and the workface undergoes such disasters such as roof collapse. To control the mining system's stability in different regions, the so-called "triunity collaborative support system" is proposed for the protection of roadway sides, workface roof, and support brackets. The above support system implementation in the three key protection areas of the lower slice will make it possible to avoid the workface's large-scale roof collapse, side falling, bracket instability, or other violation of the workface mining safety. Engineering practice has verified the feasibility of the proposed subdivision of the three key protection areas in the lower slice.

## 5. Conclusions

The physical analog modeling of the particular case study (the Huainan Panbei Coal Mine in Anhui Province, China) was used to derive the rupture characteristics and migration of the disturbed overburden in steeply inclined coal seams. The joint application of AE and fiber response techniques made it possible to draw the following conclusions:

(1) The secondary mining results in breakage and slip of the disturbed overburden hinged rock beam in the lower area and the cantilever beam in the upper area. The overburden structure is mutated, which causes the lower slice roof to break, and it is easy to induce the workface roof collapse, side falling, instability, and so forth.

(2) The lower slice's disturbed overburden experiences six stages of damage and instability, and at each stage of the broken overburden, the AE energy bundle is multimodal. The first energy peak in the AE multimodal energy bundle is the largest.

(3) The optical fiber can sense a small-scale deformation of the rock mass. The critical point where the optical fiber response develops from monotonous increasing to decreasing is roof breaking. The instantaneous strain before breaking attains its maximum value, and the overburden reaches stability when the stress is released to a minimum value. After that, as the workface advances, it is again monotonically increasing. The cycling process creates periodic pressure fluctuations along the inclined workface.

(4) During the lower slice's mining process, three key prevention and control areas, namely, the disturbed high-level immediate roof rupture, rupture of the disturbed main roof, and sliding of disturbed overburden, are observed. The AE energy per unit time in the three phases is higher than that in other breaking phases, and the rock mass fracture rate is higher, while the fiber sensing exhibits a sudden change in response value and a stepped jump increase. The research results are considered instrumental in the application of acoustic emission and fiber sensing to the deformation and damage monitoring of rock and soil structures.

## Data Availability

The data used for conducting classifications are available from the corresponding author upon request.

## Conflicts of Interest

The authors declared no potential conflicts of interest with respect to the research, authorship, and/or publication of this article.

## Acknowledgments

This work was supported by the National Natural Science Foundation of China (no. 51634007) and the Institute of Energy, Hefei Comprehensive National Science Center under Grant no. 19KZS203.

## References

[1] M. G. Qian and J. L. Xu, "Behaviors of strata movement in coal mining," *Journal of China Coal Society*, vol. 44, no. 4, pp. 973–984, 2019, in Chinese.

[2] C. O. Aksoy, H. Kose, T. Onargan, Y. Koca, and K. Heasley, "Estimation of limit angle using laminated displacement discontinuity analysis in the soma coal field, western Turkey," *International Journal of Rock Mechanics and Mining Sciences*, vol. 41, no. 4, pp. 547–556, 2004.

[3] M. Z. Gao, "Similarity model test of strata movement with steep seam," *Chinese Journal of Rock Mechanics and Engineering*, vol. 23, no. 3, pp. 441–445, 2004, in Chinese.

[4] X. Chi, K. Yang, and Q. Fu, "Analysis of regenerated roof and instability support control countermeasures in a steeply dipping working face," *Energy Exploration & Exploitation*, vol. 38, no. 4, p. 1082, 2019.

[5] J. Liu, S. L. Chen, H. J. Wang, Y. C. Li, and X. W. Geng, "The migration law of overlay rock and coal in deeply inclined coal seam with fully mechanized top coal caving," *Journal of Environmental Biology*, vol. 36, no. 4, pp. 821–827, 2015.

[6] W. Lv, Y. Wu, L. Ming, and J. Yin, "Migration law of the roof of a composited backfilling longwall face in a steeply dipping coal seam," *Minerals*, vol. 9, no. 3, p. 188, 2019.

[7] H. S. Tu, S. H. Tu, C. Zhang, L. Zhang, and X. G. Zhang, "Characteristics of the roof behaviors and mine pressure manifestations during the mining of steep coal seam," *Archives of Mining Sciences*, vol. 62, no. 4, pp. 871–891, 2017.

[8] Y. P. Wu, P. S. Xie, and S. G. Ren, "Analysis of asymmetric structure around coal face of steeply dipping seam mining," *Journal of China Coal Society*, vol. 35, no. 2, pp. 182–184, 2010, in Chinese.

[9] P. S. Xie, S. Q. Tian, and J. J. Duan, "Experimental study on the movement law of roof in pitching oblique mining area of steeply dipping seam," *Journal of China Coal Society*, vol. 44, no. 10, pp. 2974–2982, 2019, in Chinese.

[10] Q. Guo, J. Pan, M. Cai, and Y. Zhang, "Investigating the effect of rock bridge on the stability of locked section slopes by the direct shear test and acoustic emission technique," *Sensors*, vol. 20, no. 3, p. 638, 2020.

[11] Q. Guo, J. Pan, M. Cai, and Y. Zhang, "Analysis of progressive failure mechanism of rock slope with locked section based on energy theory," *Energies*, vol. 13, no. 5, p. 1128, 2020.

[12] X. P. Lai, H. Sun, P. F. Shan, C. L. Wang, N. Cui, and Y. R. Yang, "Acoustic emission and temperature variation in failure process of hard rock pillars sandwiched between thick coal seams extremely steep," *Chinese Journal of Rock Mechanics and Engineering*, vol. 34, no. 11, pp. 2285–2292, 2015, in Chinese.

[13] X. P. Lai, Y. R. Yang, N. B. Wang, P. F. Shan, and D. F. Zhang, "Comprehensive analysis to temporal-spatial variation of dynamic instability of steeply inclined coal-rock mass," *Chinese Journal of Rock Mechanics and Engineering*, vol. 37, no. 3, pp. 583–592, 2018, in Chinese.

[14] H. W. Wang, M. M. Shao, G. Wang, and D. X. Deng, "Characteristics of stress evolution on the thrust fault plane during the coal mining," *Journal of China Coal Society*, vol. 44, no. 8, pp. 2318–2327, 2019, in Chinese.

[15] K. Yang, X. L. Chi, Q. J. Liu, W. J. Liu, and S. Liu, "Research on cataclastic regenerated roof and instability mechanism of support in fully mechanized mining face of steeply dipping seam," *Journal of China Coal Society*, vol. 20, pp. 1–10, 2020, in Chinese.

[16] S. K. Zhao, "Experiments on the characteristics of thrust fault activation influenced by mining operation," *Journal of Mining and Safety Engineering*, vol. 33, no. 2, pp. 354–360, 2016, in Chinese.

[17] L. J. Butler, N. Gibbons, P. He, C. Middleton, and M. Z. E. B. Elshafie, "Evaluating the early-age behaviour of full-scale prestressed concrete beams using distributed and discrete fibre optic sensors," *Construction and Building Materials*, vol. 126, pp. 894–912, 2016.

[18] A. Klar, I. Dromy, and R. Linker, "Monitoring tunneling induced ground displacements using distributed fiber-optic sensing," *Tunnelling and Underground Space Technology*, vol. 40, no. 2, pp. 141–150, 2014.

[19] X. Jiang, Y. Gao, Y. Wu, and M. Lei, "Use of brillouin optical time domain reflectometry to monitor soil-cave and sinkhole formation," *Environmental Earth Sciences*, vol. 75, no. 3, pp. 1–8, 2016.

[20] H.-H. Zhu, B. Shi, J.-F. Yan, J. Zhang, and J. Wang, "Investigation of the evolutionary process of a reinforced model slope using a fiber-optic monitoring network," *Engineering Geology*, vol. 186, pp. 34–43, 2015.

[21] M. Kihara, K. Hiramatsu, M. Shima, and S. Ikeda, "Distributed optical fiber strain sensor for detecting river embankment collapse," *Ice Transactions on Electronics*, vol. 85, no. 4, pp. 952–960, 2002.

[22] Y. Qiu, Q.-B. Wang, H.-T. Zhao, J.-A. Chen, and Y.-Y. Wang, "Review on composite structural health monitoring based on fiber bragg grating sensing principle," *Journal of Shanghai Jiaotong University (Science)*, vol. 18, no. 2, pp. 129–139, 2013.

[23] A. Klar and R. Linker, "Feasibility study of automated detection of tunnel excavation by brillouin optical time domain reflectometry," *Tunnelling and Underground Space Technology*, vol. 25, no. 5, pp. 575–586, 2010.

[24] J. Chai, Y. Y. Sun, Y. Y. Qian, J. Song, W. C. Ma, and Y. Li, "Strata movement testing based on FBG-BOTDA combined sensing technology in similar model," *Journal of Xian University of Science and Technology*, vol. 36, no. 1, pp. 1–7, 2016, in Chinese.

[25] J. Chai, Q. Liu, J. Liu, and D. Zhang, "Optical fiber sensors based on novel polyimide for humidity monitoring of building materials," *Optical Fiber Technology*, vol. 41, pp. 40–47, 2018.

[26] J. Chai, Y. Y. Yang, Y. B. Ouyang, D. D. Zhang, W. G. Du, and S. J. Li, "Comparative study of optical measurement methods for deformation and failure simulation test of overburden in stope," *Journal of China Coal Society*, vol. 47, pp. 1–11, 2020, in Chinese.

[27] Y. Liu, W. Li, J. He, S. Liu, L. Cai, and G. Cheng, "Application of brillouin optical time domain reflectometry to dynamic monitoring of overburden deformation and failure caused by underground mining," *International Journal of Rock Mechanics and Mining Sciences*, vol. 106, pp. 133–143, 2018.

[28] B. Madjdabadi, B. Valley, M. B. Dusseault, and P. K. Kaiser, "Experimental evaluation of a distributed brillouin sensing system for detection of relative movement of rock blocks in underground mining," *International Journal of Rock Mechanics and Mining Sciences*, vol. 93, pp. 138–151, 2017.

[29] K. Kishida, C. H. Li, S. B. Liu, and K. Nishiguchi, "Pulse prepump method to achieve cm-order spatial resolution in brillouin distributed measuring technique," *IEICE Technical Report*, vol. 47, pp. 15–20, 2004.

[30] B. Ghabraie, G. Ren, X. Zhang, and J. Smith, "Physical modelling of subsidence from sequential extraction of partially overlapping longwall panels and study of substrata movement characteristics," *International Journal of Coal Geology*, vol. 140, pp. 71–83, 2015.

[31] W. S. Zhu, Y. Li, S. C. Li, S. G. Wang, and Q. B. Zhang, "Quasi-three-dimensional physical model tests on a cavern complex under high in-situ stresses," *International Journal of Rock Mechanics and Mining Sciences*, vol. 48, no. 2, pp. 199–209, 2011.

[32] W. B. Suo, B. Shi, W. Zhang, H. L. Cui, J. Liu, and J. Q. Gao, "Study on calibration of distributed optical fiber sensors based on BOTDR," *Chinese Journal of Scientific Instrument*, vol. 27, no. 9, pp. 985–989, 2006, in Chinese.

[33] X. Xi, S. Yang, and C.-Q. Li, "A non-uniform corrosion model and meso-scale fracture modelling of concrete," *Cement and Concrete Research*, vol. 108, pp. 87–102, 2018.

[34] X. Xi, S. Yang, C.-Q. Li, M. Cai, X. Hu, and Z. K. Shipton, "Meso-scale mixed-mode fracture modelling of reinforced concrete structures subjected to non-uniform corrosion," *Engineering Fracture Mechanics*, vol. 199, pp. 114–130, 2018.